



HAL
open science

Mesostructured cellular foam silica supported Au-Pt nanoalloy: enrichment of d-state electrons for promoting the catalytic synergy

Pingping Wu, Haijun Liu, Yunxiang Cao, Shibo Xi, Zhiheng Li, Zhengke He, Lei Song, Jing Xu, Peng Bai, Lianming Zhao, et al.

► To cite this version:

Pingping Wu, Haijun Liu, Yunxiang Cao, Shibo Xi, Zhiheng Li, et al.. Mesostructured cellular foam silica supported Au-Pt nanoalloy: enrichment of d-state electrons for promoting the catalytic synergy. *Microporous and Mesoporous Materials*, 2021, 316, pp.110982. 10.1016/j.micromeso.2021.110982 . hal-03150726

HAL Id: hal-03150726

<https://hal.science/hal-03150726>

Submitted on 24 Feb 2021

HAL is a multi-disciplinary open access archive for the deposit and dissemination of scientific research documents, whether they are published or not. The documents may come from teaching and research institutions in France or abroad, or from public or private research centers.

L'archive ouverte pluridisciplinaire **HAL**, est destinée au dépôt et à la diffusion de documents scientifiques de niveau recherche, publiés ou non, émanant des établissements d'enseignement et de recherche français ou étrangers, des laboratoires publics ou privés.

Mesostructured cellular foam silica supported Au-Pt nanoalloy: enrichment of d-state electrons for promoting the catalytic synergy

Pingping Wu^a, Haijun Liu^b, Yunxiang Cao^a, Shibo Xi^c, Zhiheng Li^a, Zhengke He^a, Lei Song^a, Jing Xu^b, Peng Bai^{a*}, Lianming Zhao^{b*}, Svetlana Mintova^{a,d}, Zifeng Yan^a

^a *State Key Laboratory of Heavy Oil Processing, Key Laboratory of Catalysis, College of Chemical Engineering, China University of Petroleum (East China), Qingdao 266580, China*

^b *School of Materials Science and Engineering, Institute of Advanced Materials, China University of Petroleum (East China), Qingdao 266580, China*

^c *Institute of Chemical and Engineering Sciences, A*Star, 1 Pesek Road, 627833, Singapore*

^d *Normandie University, ENSICAEN, UNICAEN, CNRS, Laboratoire Catalyse et Spectrochimie, 14000 Caen, France*

* Corresponding authors. Tel: +86-532-86981812

E-mail address: baipeng@upc.edu.cn (P. Bai); lmzhao@upc.edu.cn (L. Zhao)

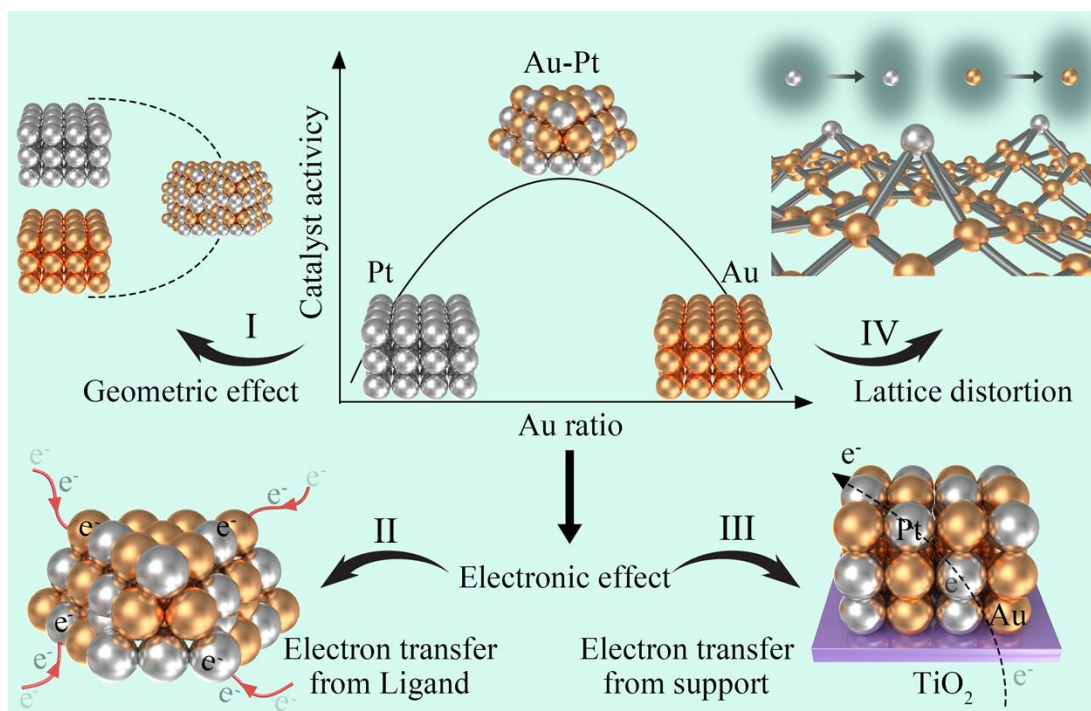
ABSTRACT

A mesostructured cellular foam (MCF) silica was applied to support gold (Au) – platinum (Pt) alloy nanoparticles (NPs) for benzyl alcohol partial oxidation. A catalytic synergy on bimetallic gold (Au)-platinum (Pt) nanoparticle (NP) catalyst, referring to that introducing Au to Pt leading to a higher catalytic performance has been observed. However, the essence of this synergistic effect is still under debate. In this work, a series of MCF supported Au-Pt NP catalysts are designed to reveal the essence. Well-developed porous structure of MCF support eliminated the mass transfer limitation and intrinsic catalytic activity was obtained. The improved catalytic performance on bimetallic catalyst is attributed to the geometric and electronic changes of active sites after formation of Au-Pt alloy NPs. Compared with monometallic catalyst, the formation of Au-Pt alloy results in the changes of particle size and lattice structure. Electronic property analyses confirmed the increase of d state electrons on Au-Pt alloy NPs, which are calculated from s-p-d hybridization and intra-atomic charge redistribution, leading to the increased abundance of transferable d electrons near Fermi level and further enhancing the catalytic activity. These findings gain new insights into the catalytic synergy of bimetallic nanoparticles and shed light on the optimization of these catalysts.

Keywords: Mesostructured cellular foam silica; Au-Pt bimetallic catalyst; promoter effect; benzyl alcohol partial oxidation

1. Introduction

Noble metal nanoparticles (NPs) such as Au, Pt, Pd, Ru, Rh are receiving extensive attention due to their important applications in heterogeneous catalysis [1-4], sensors [5, 6], electronics [7-9] and biology [10, 11]. In the case of catalysts based on noble metal nanoparticles, two important aspects were usually investigated, geometrical and electronic effects, which are related to particle size [12], metal-support interactions [13-15], chemical compositions [16, 17], promoter effects [18, 19], etc. It is an effective strategy to optimize the performance of catalysts through the variation of these two distinctive effects. Among various catalytic applications, supported noble metal NPs, especially Au, Pt, Pd, have been widely applied to partial oxidation reactions during the past decade [20-24]. It has been frequently reported that the formation of bimetallic alloy NPs after introducing another metal as a promoter leads to a higher catalytic activity and/or selectivity [18, 25-27]. A catalytic synergy was observed on Au-Pd/CeZrO₂ catalyst for benzyl alcohol oxidation, which was ascribed to the electronic interaction between Au and Pd atoms [28]. In our previous work, the activity enhancement on Au-Pd bimetallic catalyst was achieved, which was attributed to the variation of surface chemical state, and the alloying of Au-Pd retarded the formation of inert PdO species on the surface of alloy particles [29]. Chen and co-workers observed the migration of Pd onto Au particles, resulting in the formation of Au@Pd or AuPd@Pd core shell nanostructures with high activity in the benzyl alcohol oxidation [25].



Scheme 1 Proposed explanations for catalytic synergy in Au-Pt bimetallic catalysts [30-33].

Similar catalytic synergy was also observed on Au-Pt bimetallic catalysts [30-32]. Besson and co-workers found that alloying Au with Pt in Au-Pt/C catalyst improved its catalytic activity and selectivity for 1,6-hexanediol oxidation to adipic acid [31]. A higher catalytic activity for the selective aerobic oxidation of polyols was obtained on catalyst Pt₆₀Au₄₀-starch/HT than that on monometallic Pt-starch/HT or Au-starch/HT [32]. Amal and co-workers also observed the occurrence of catalytic synergy on bimetallic Au-Pt/TiO₂ catalyst, and a UV light pre-treatment was applied to enhance this effect [30]. The catalytic synergy between Au and Pt was commonly explained as geometric and electronic effect as shown in Scheme 1. Mavrikakis and Herron [34] found that a Pt-overlayer is thermodynamically preferred on PtAu alloy upon oxygen adsorption

by applying self-consistent density functional theory calculations. The surface Pt segregation in bimetallic Pt-Au alloy surfaces at O₂ atmosphere is considered as an important factor of geometric effect during oxidation reaction. Bokhoven and Bus explained that the electronic effect originated from the interatomic charge transfer from the Au 5d to the Pt 5d band, accompanied by intra-atomic charge re-distribution [33]. Based on the work function difference between Au (5.1 eV) and Pt (5.65 eV), Pt was supposed to abstract electrons from Au in homogeneous Au-Pt alloy NPs, which would result in an electron density loss in Au and an electron density gain in Pt, corresponding to a positive shift of Au 4f binding energy (BE) and a negative shift of Pt 4f BE in the XPS spectra. However, quite unexpectedly, researchers have observed negative shifts in BEs of both Au 4f and Pt 4f [30, 32, 35]. These negative shifts were commonly ascribed to the increased electron density in both elements. Amal et al attributed these negative shifts as electron transfer from TiO₂ support to Au and Pt atoms, however, no positive shift in the Ti 2p BE was observed [30]. Tongsakul and co-workers [32] postulated that these negative shifts were attributed to electron transfer both from starch ligand to Au and Pt atoms and from Au to Pt on Pt_xAu_y-starch/HT catalysts, and no experimental or theoretical evidences were provided. Later, a charge compensation model was applied by Wang and coworkers to investigate the electronic structure of Au-Pt bimetallic alloy, the negative shifts of both Au and Pt 4f were attributed to the s-d hybridization and charge compensation [35]. In our previous work, no ligand was present after high temperature calcination, and the negative

shifts in both Au and Pt 4f BEs were also observed on Au-Pt/SiO₂ catalysts [36]. Therefore, the negative shifts in both Au and Pt 4f BEs appear to be a common phenomenon in the Au-Pt alloy NPs. Hence, it is important to understand this phenomenon, which may clarify the essence of the catalytic synergy of bimetallic Au-Pt alloy NP catalysts.

As can be envisaged, the interaction between Au and Pt atom nucleus occurs during the alloying process, which may lead to the polarization of the electron clouds, thus possibly influencing the electronic state of both atoms. Moreover, the high availability of electrons near the Fermi level can enhance surface phenomena in heterogeneous catalysis [37]. Thus, the catalytic synergy on Au-Pt alloy NPs may be closely related to the available electrons near the Fermi level. However, more experimental and theoretical investigations are needed to clarify this fundamental issue. In this work, we designed a series of mesoporous silica supported Au-Pt NPs catalysts with different Au/Pt ratios through a one-pot synthesis method. Direct experimental evidences were provided for the increased density of transferable d-orbital electrons in Au-Pt NPs, which correlated well with the enhanced catalytic activity after alloying. The density function theory (DFT) calculations were performed to understand the surface electronic properties of Au-Pt alloy NPs. Combining the experimental and theoretical results, the essence of surface electronic variation and the corresponding catalytic synergy in Au-Pt alloy NPs was clarified.

2. Experimental

2.1. Chemicals

Triblock co-polymer PEO₂₀PPO₇₀PEO₂₀ (P123) and mercaptopropyltrimethoxysilane (MPTMS, 97%) were purchased from Aldrich. H₂AuCl₄·xH₂O, H₂PtCl₆·6H₂O, tetraethyl orthosilicate (TEOS, 98%), hydrochloric acid (37%), benzyl alcohol (99.99%), benzaldehyde (99.99%), benzoic acid (99.99%) and absolute ethanol (99.98%) were purchased from Sinopharm Chemical. All chemicals were used as received without further purification.

2.2. Preparation of catalysts

A mesostructured cellular foam (MCF) silica was applied as matrix to support Au-Pt NPs and the catalysts were prepared following a one-pot synthesis procedure as previously reported by us [29]. In a typical synthesis, 4 g of P123 was dissolved in a mixture of 65 mL of deionized water and 5 mL of 37% HCl at room temperature. Then, 3 g of 1,3,5-trimethylbenzene was added into the clear solution as a pore swelling agent and stirred at 40 °C for 2 h, followed by dropwise addition of 8.32 g TEOS and 0.78 g MPTMS into the mixture. Finally, H₂AuCl₄ and H₂PtCl₄ (total metal loading of 1 wt. %) solutions were introduced to the synthesis system. After stirring at 40 °C for 24 h, the mixture was transferred to a Teflon-lined stainless-steel autoclave to undergo a hydrothermal treatment at 100 °C for 24 h. The solids were filtered off, washed with deionized water, vacuum dried at 80 °C overnight and calcined in air at 500 °C for 6 h. Finally, the calcined samples were reduced in H₂ atmosphere at 300 °C for 2 h. The obtained catalysts are denoted as Au_xPt_y/MCF, where *x*, *y* represent the

molar percentages of Au and Pt from ICP analysis, respectively, with a total metal weight loading of 1wt.%.

2.3. Characterization

X-ray powder diffraction (XRD) patterns of catalysts were recorded on a X'Pert PRO MPD system with a Cu $K\alpha$ radiation ($\lambda = 0.154$ nm) at 35 kV and 40 mA. N_2 adsorption/desorption was carried out at -196 °C using an automatic volumetric sorption analyzer (Micromeritics, TriStar 3000) after degassing at 300 °C for 4 h under vacuum. The specific surface area was calculated using the Brunauer-Emmett-Teller (BET) equation in the relative pressure range of 0.05-0.25. The total pore volume of catalysts was obtained at the relative pressure P/P_0 of 0.998. The cell sizes of MCF silica supported Au-Pt catalysts were determined by applying the Broekhoff-de Boer-Frenkel-Halsey-Hill (BdB-FHH) method [38] from nitrogen adsorption branches. The metals loading in the catalysts was determined by inductively coupled plasma optical emission spectroscopy (ICP-OES) using a VISTA-MPX Varian system. The microstructure of the catalysts was characterized by high-resolution transmission electron microscopy (HRTEM) using a JEOL JEM 2010 microscope operated at 200 kV. Based on the TEM images of the Au-Pt bimetallic catalysts, diameters of more than 200 randomly selected metal particles were measured, and the average particle diameter was calculated based on following equation: $d = \sum n_i d_i / \sum n_i$, where $n_i \geq 200$. The metal dispersion was calculated using GAUSS software from Nanomaterials and Catalysis Group of University of Cadiz (Spain) assuming a spherical particle shape [39]. Scanning transmission electron

microscopy (STEM) high angle annular dark field (HAADF) images and X-ray energy dispersive spectra (XEDS) were applied to analyze the element distribution of bimetallic NPs. The solid-state ultraviolet-visible (UV-vis) spectra of catalysts were measured on a Hitachi U-4100 UV-vis-NIR spectrophotometer using BaSO₄ as an internal reference. The diffuse reflectance spectra from 200 to 800 nm were recorded. The X-Ray Photoelectron Spectroscopy (XPS) analyses were performed on a Thermo-VG Scientific K-Alpha spectrometer equipped with an Al anode (Al $K\alpha$ = 1486.6 eV). C 1s electron binding energy corresponding to graphitic carbon at 284.5 eV was applied as a calibration binding energy reference.

In situ diffuse reflectance infrared Fourier transformed (DRIFT)spectroscopy study using CO probe molecule (CO-FT-IR) on fresh catalysts (pretreated in H₂ at 300 °C with a flow rate of 20 mL min⁻¹ for 60 min, cooled down to 30 °C and purged with He for 30 min) was conducted in a high temperature diffuse reflectance cell (PIKE). The spectra were recorded on a BRUKER VERTEX70 FT-IR spectrometer at room temperature in the range of 400-4000cm⁻¹with a resolution of 4 cm⁻¹. Extended X-ray absorption fine structure (EXAFS) and X-ray absorption near edge structure spectra (XANES) were collected at the XAFCA beamline of Singapore Synchrotron Light Source [40]. The measurements were carried out using a Si (111) double-crystal monochromator. The size of the beam at the sample position was *ca.* 2 mm (h) × 1 mm (v). Samples were measured in vacuum chamber. The data were collected both in fluorescence mode, by means of a silicon drift detector (Bruker XFlash 6|100), and in transmission mode simultaneously. The ion chamber before the sample was used for

measurement of incoming photons. Data were normalized using the Athena program with a linear pre-edge and polynomial post-edge background subtracted from the raw data [40]. EXAFS fits were performed using ARTEMIS software [41]. The interatomic distances were optimized by fitting the experimental data.

2.4. Catalytic test

The solvent-free aerobic oxidation of benzyl alcohol with O₂ was conducted in a 100 mL autoclave with a polytetrafluoroethylene liner (Model: SLM100, Beijing Easychem Science and Technology Development Company, China). In a typical reaction, 0.1 mol of benzyl alcohol was introduced into the reactor followed by adding 50 mg of solid catalyst. After purging with O₂ for three times, the reactor was heated to 110 °C and the O₂ pressure was adjusted to 0.8 MPa under stirring. The O₂ pressure was maintained at 0.8 MPa throughout the reaction. After 1 h of reaction, the reactor was cooled down to room temperature and the pressure was released. Finally, the reactor was opened and the products were separated by centrifugation. The n-pentanol was added to the reaction products as an internal standard. Finally, the reaction products were analysed using a gas chromatogram (Agilent 6870) equipped with a flame ionization detector (FID) and a DB-1 column (30*0.32*0.25). The turnover frequency (TOF) was calculated based on moles of benzyl alcohol converted per mole of surface metals (Au + Pt) or Pt per hour, e.g., $M_{\text{BA converted}} \text{ h}^{-1} M_{\text{surface metal}}^{-1}$, while the amount of surface metals (Au + Pt) or Pt was calculated based on the total moles of metals multiplied by the metal dispersion.

2.5. Theoretical calculation

The Au, Pt and Au-Pt alloy NPs catalysts were simulated using 55 atoms (Au_{55} , Pt_{55} , $\text{Au}_{40}\text{Pt}_{15}$ and $\text{Au}_{15}\text{Pt}_{40}$) models and also the Au(111) Au₃Pt(111), AuPt₃(111), and Pt(111) surfaces to eliminate the size effect. The surface model was established by a four-layers periodic slab model with a $p(4\times 4)$ unit cell and a vacuum region of 15 Å. The geometric structures of all the cluster and surface models were optimized by using the spin-polarized DFT in the DMol³ package [42, 43]. The exchange-correlation term was treated by the general gradient approximation (GGA) method with the Perdew–Burke–Ernzerhof (PBE) functional [44]. In addition, the Grimme method for DFT-D correction (PBE + D2) was used to describe the van der Waals interactions [45]. The localized double-numerical basis with polarization (DNP) function was selected as the basis set [46]. The density functional semicore pseudopotential (DSPP) method was used for the relativistic effect. The value of global orbital cutoff was chosen to be 4.9 Å. The tolerances of energy, gradient, and displacement convergence were 1×10^{-5} Ha, 2×10^{-3} Ha/Å, and 5×10^{-3} Å, respectively.

The projected density of states (PDOS) for Au and Pt atoms in the 55 atoms NPs were calculated by CASTEP code with a cutoff energy of 571 eV [47]. The OTFG ultrasoft pseudopotential was chosen in calculation, which provides results in close agreement with all electron calculation and is very accurate for describing ground state structure [48]. The other details were consistent with the above DMol³ computations. To explore valence electron distribution, the occupancies (N) of the s, p,

d electrons in the valence band range were calculated by the integral of the corresponding density of states from about -10 eV to the Fermi level. In addition, the PDOS for Au and Pt atoms in the Au(111) Au₃Pt(111), AuPt₃(111), and Pt(111) surfaces were also calculated to eliminate the size effect during the calculation.

The net charge density (ρ_{Net}) of the catalyst surfaces is calculated by :

$$\rho_{\text{net}} = \frac{\sum_{i=1}^{n_{\text{Au}}} q_{\text{Au}} + \sum_{j=1}^{n_{\text{Pt}}} q_{\text{Pt}}}{(n_{\text{Au}} + n_{\text{Pt}})S}$$

where q_{Au} and q_{Pt} are the charges of the Au and Pt atoms in the surfaces, respectively; n_{Au} and n_{Pt} are the numbers of the Au and Pt atoms in the surface, respectively; S is the surface area of the catalyst.

The adsorption energy (E_{ads}) of an adsorbate on catalyst surfaces was defined as

$$E_{\text{ads}} = E_{\text{adsorbate/substrate}} - (E_{\text{adsorbate}} + E_{\text{substrate}}),$$

where $E_{\text{adsorbate/substrate}}$ and $E_{\text{substrate}}$ correspond to the total energy of the catalyst substrate with and without an adsorbed molecule, respectively; while $E_{\text{adsorbate}}$ represents the energy of the free adsorbate.

3. Results and discussion

3.1. Catalytic performance

The catalytic performances of Au_xPt_y/MCF catalysts for benzyl alcohol oxidation were evaluated. The catalytic activity and benzaldehyde selectivity are shown in Fig.1; detailed catalytic results and metal dispersions are summarized in Table S1. The blank reaction was carried out under the same reaction conditions without a catalyst, a low benzyl alcohol conversion (2.1%) was obtained with a relative low benzaldehyde selectivity of 45.6%. Mono-metallic catalyst Pt₁₀₀/MCF exhibited a much higher

catalytic activity (TOF=30000 h⁻¹) than that of catalyst Au₁₀₀/MCF (TOF=4900 h⁻¹). Catalyst Au₁₀₀/MCF exhibited the lowest benzyl alcohol conversion (4.9%) and the lowest benzaldehyde selectivity (47.2%) among all catalysts, which is probably due to its inert catalytic activity to benzyl alcohol activation [30]. The highest catalytic activity (TOF = 37000 h⁻¹) was obtained on catalyst Au₁₉Pt₈₁/MCF with a relatively high benzaldehyde selectivity of 93.3%, which is probably due to the formation of Au-Pt alloy NPs. Among Au-Pt bimetallic catalysts, the catalytic activity increased with the increase of Pt content, while the benzaldehyde selectivity exhibited a reverse trend. As shown in Table S1, the TOFs calculated based on Pt revealed that the catalytic activity increased with the decrease of Pt ratio, indicating the catalytic synergy on bimetallic Au-Pt NP catalyst. This is in good consistence with literature results [30-32] which was previous ascribed to either size or electronic effect of metal NPs. However, the actual mechanism of this catalytic synergy is still under debate and no satisfactory theoretical explanation is achieved to interpret the alloying effects on the reactant activation or reaction process. The obtained catalyst Au₁₉Pt₈₁/MCF exhibited excellent stability for 6 consecutive reactions of the same catalyst after regeneration as shown in Fig. S1, and no obvious leaching of metal components was detected (shown in the last row of Table 1). This is because the partial encapsulation of Au-Pt alloy NPs in the silica matrix inhibits the sintering/leaching of noble metal NPs during reaction. The partial encapsulation of Au-Pt alloy NPs in the silica matrix was deduced from our previous work which applied similar one-pot preparation method and same functional ligand for supported Au-Pd alloy NPs synthesis, and both

TEM and 3D electron tomography analysis revealed the partial encapsulation of Au-Pd alloy NPs in silica support [29].

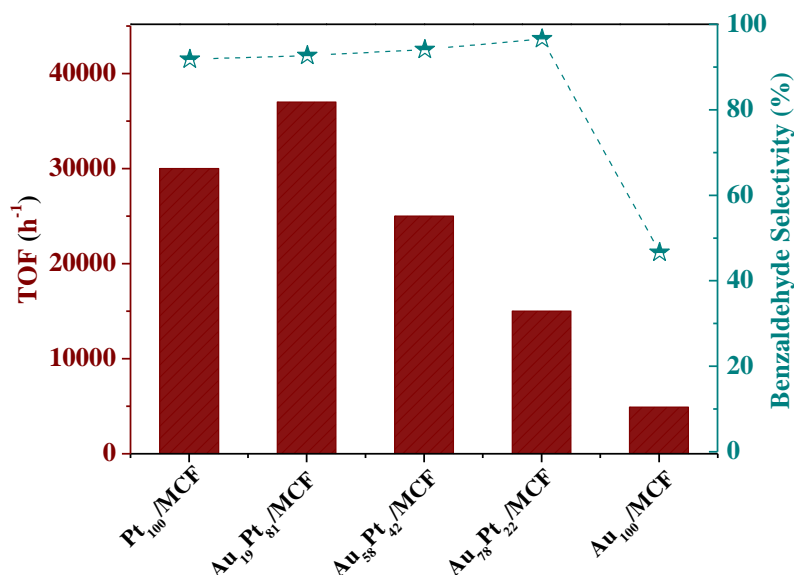


Fig. 1. Catalytic activity and benzaldehyde selectivity on Au_xPt_y/MCF catalysts

(Reaction conditions : 50 mg of catalyst, 110 °C for 1 h under an O₂ pressure of 8 bars. The TOF was calculated based on moles of benzyl alcohol converted per mole of surface metals (Au + Pt) per hour.)

To eliminate the effect of mass transfer limitations, benzyl alcohol partial oxidation was performed on catalyst Au₁₉Pt₈₁/MCF at 110°C in a batch reactor with different catalyst particle sizes (as shown in Fig. S2). The calculation was carried out with Mears criterion for eliminating the external diffusion limitation $\frac{-r'_A \rho_b Rn}{k_c C_{Ab}} < 0.15$

[49] and Weisz–Prater criterion $C_{WP} = \frac{-r'_{A(obs)} \rho_c R^2}{D_e C_{As}} < 1$ for eliminating internal

diffusion limitation [50], and the details of the calculation process are provided in the supplementary information. Under the reaction conditions, for the Mears criterion,

$\frac{-r_A' \rho_b Rn}{k_c C_{Ab}}$ was calculated to be 9.32×10^{-4} , which is lower than 0.15, indicating that

no external diffusion limitations exist. For the Weisz–Prater criterion, C_{wp} was calculated to be $1.18 \times 10^{-4} < 1$, indicating that no internal diffusion limitations exist [51]. Besides, for the slurry bed reactor with a stirring rate of 800-1000 rpm, the heat transfer limitation is negligible.

3.2. Catalysts characterization

The detailed physicochemical properties of Au-Pt bimetallic catalysts are summarized in Table 1. The total metal (Au+Pt) loading of all catalysts is constant, i.e. in the range of 0.8-1.0wt.%. XRD patterns of catalysts are shown in Fig. S3a. After introducing Au to Pt catalyst, the diffraction peaks of the cubic Pt are shifted to lower angles and the peaks are located between the peaks assigned to pure Au and Pt, implying the formation of Au-Pt alloy NPs. As shown in Table 1, the values of lattice constants of bimetallic catalysts are between those of the monometallic Au and Pt. The lattice constant increased from 0.2618 nm (Pt₁₀₀/MCF) to 0.2673 nm (Au₇₈Pt₂₂/MCF) with the increase of Au/Pt ratio, thus revealing the formation of Au-Pt alloy NPs and incorporation of Au into Pt lattice. As has been reported, the lattice structure variation between Au and Pt usually causes a lattice contraction of Au and a lattice expansion of Pt in the bimetallic NPs [32]. The increase of Pt lattice constant will weaken/distort Pt–Pt bonds and may generate non-bonding electrons [33], which may significantly influence the catalyst performance. The formation of Au-Pt alloy NPs was further justified by solid-state UV-vis analysis (Fig. S3b).

The UV-vis spectrum of catalyst Au₁₀₀/MCF contains a band at 520 nm (see inset of Fig. S3b) corresponding to the surface plasmon resonance (SPR) of Au⁰ NPs [52], while the broad peak at 420 nm is usually assigned to Au_n clusters [53]. No surface plasmon resonance peak was observed on catalyst Pt₁₀₀/MCF as expected in the range of 200 - 800 nm. After introducing Pt to Au catalyst, the SPR peak of Au⁰ NPs became broader or even disappeared with the increase of Pt content. This indicates the surface electronic variation of Au NPs after introducing Pt, and this was attributed to the formation of Au-Pt alloy NPs.

Table 1

Textural properties of catalysts

Samples	Au Loading ^b (wt.%)	Pt Loading ^b (wt.%)	d_{111} (nm)	a_0 (nm)	S_{BET} (m ² /g)	Pore volume (cm ³ /g)	Cell diameter (nm)	Window diameter (nm) [54-56]	Average particle size (nm) ^c
Pt ₁₀₀ /MCF	-	0.89	0.2267	0.2618	707	0.98	13.7	<5-6	9.6
Au ₁₉ Pt ₈₁ /MCF	0.16	0.67	0.2270	0.2621	709	1.03	16.9	<5-6	6.6
Au ₅₈ Pt ₄₂ /MCF	0.49	0.36	0.2290	0.2644	707	0.98	16.9	<5-6	5.6
Au ₇₈ Pt ₂₂ /MCF	0.68	0.19	0.2315	0.2673	738	1.05	14.2	<5-6	4.4
Au ₁₀₀ /MCF	0.96	-	0.2353	0.2717	696	1.00	12.5	<5-6	2.7
Au ₁₉ Pt ₈₁ /MCF ^a	0.17	0.65	0.2271	0.2621	685	1.00	12.2	<5-6	6.7

^a Physical and chemical properties of catalyst Au₁₉Pt₈₁/MCF after 6th cycle reaction.

^b The metal loading was evaluated by ICP-OES.

^c The average particle diameter was calculated based on TEM images of the Au-Pt bimetallic catalysts, following equation: $d = \sum ni d_i / \sum ni$, where $ni \geq 200$.

S_{BET} , surface area calculated by the BET method. V_{total} , total pore volume calculated at $P/P_o = 0.998$.

The cell diameters of Au-Pt catalysts were determined by applying the Broekhoff–de Boer-Frenkel–Halsey–Hill method from nitrogen adsorption branches.

$$a_0 = 2d_{111} / \sqrt{3}$$

The textural properties of $\text{Au}_x\text{Pt}_y/\text{MCF}$ catalysts were characterized by N_2 adsorption-desorption analysis. The N_2 sorption isotherms of Au-Pt bimetallic catalysts are shown in Fig. S3c. All catalysts exhibit a type-IV isotherm with a H-2 hysteresis loop, indicating the presence of ink-bottle type mesopores. The cell diameters of Au-Pt catalysts were determined by applying the BdB-FHH method from nitrogen adsorption branches [38], the pore size distribution curves are shown in Fig. S4 and the textural properties are summarized in Table 1. The very steep desorption branch and the closure point of the hysteresis loop at lower $P/P_0 \sim 0.45$ suggests the cavitation-controlled evaporation with window sizes of $<5\text{--}6$ nm [54-56]. The cell diameters are in the range of 12-20 nm and the window diameters are smaller than 5-6 nm [54]. No obvious difference of the textural properties (specific surface area, pore volume and pore size) of these Au-Pt bimetallic catalysts with different Au/Pt ratios was observed, probably due to the low metals loading (~ 1.0 wt.%) [21]. Well-developed porous structure of MCF support would eliminate the mass transfer limitation and intrinsic catalytic activity was obtained.

The TEM and STEM-HAADF images revealing the size of the particles and metals distribution in the catalysts are shown Fig. 2. Pure $\text{Pt}_{100}/\text{MCF}$ exhibits the largest size of metal NP in the range of 6-13 nm (average particle size of 9.6 nm), while $\text{Au}_{100}/\text{MCF}$ contains the smallest size of metal NP in the range of 1-5 nm (average particle size of 2.7 nm) among all catalysts. The size of metal NP decreased with the increase of Au/Pt ratio in the catalysts, which is due to the formation of bimetallic Au-Pt alloy NPs, hampering their further aggregation during the one-pot

synthesis. The representative interplanar spacing of Au-Pt (111) phase (0.2295 nm) measured from TEM image on catalyst Au₁₉Pt₈₁/MCF (inset image) confirmed the lattice contraction of Au (111) (0.2353 nm) and the lattice expansion of Pt (111) (0.2267 nm), which is in a good accordance with the XRD results. For the pure Au catalyst, the size of Au NPs has been considered as a main factor that govern the catalyst activity [12]. Catalysts with smaller size of NPs usually exhibited better catalytic activity due to the presence of more low-coordinated active sites exposed to reactants [21]. However, in this work, catalyst Au₁₀₀/MCF with the smallest average particle size of 2.7 nm shows the lowest catalytic activity (TOF = 4900 h⁻¹) shown in Table S1, which was due to its inert catalytic activity to alcohol oxidative dehydrogenation and H-abstraction, the critical steps for benzyl alcohol activation [57, 58]. In contrast, catalyst Pt₁₀₀/MCF with the largest size of metal NP in the range of 6-13 nm exhibited a relative high benzyl alcohol activity (TOF = 30000h⁻¹), while the highest catalytic activity (TOF = 37000h⁻¹) was obtained for catalyst Au₁₉Pt₈₁/MCF with NP size in the range of 4-10 nm. This indicates that introducing a small amount of Au to Pt led to a higher metal dispersion on catalyst Au₁₉Pt₈₁/MCF, resulting in a higher catalytic activity than that of the monometallic Pt₁₀₀/MCF catalyst. Since the other two bimetallic catalysts Au₅₈Pt₄₂/MCF and Au₇₈Pt₄₂/MCF with higher metal dispersions exhibit a lower catalytic activity than the Au₁₉Pt₈₁/MCF, one can conclude that the metal dispersion is clearly not the main factor determining the activity of bimetallic Au-Pt catalysts. In summary, Pt is the predominant active component for benzyl alcohol oxidation in Au-Pt bimetallic

catalyst, and the introduction of Au improved the Pt dispersion, however which is not the main reason for the improvement of catalytic activity of Au-Pt bimetallic catalyst.

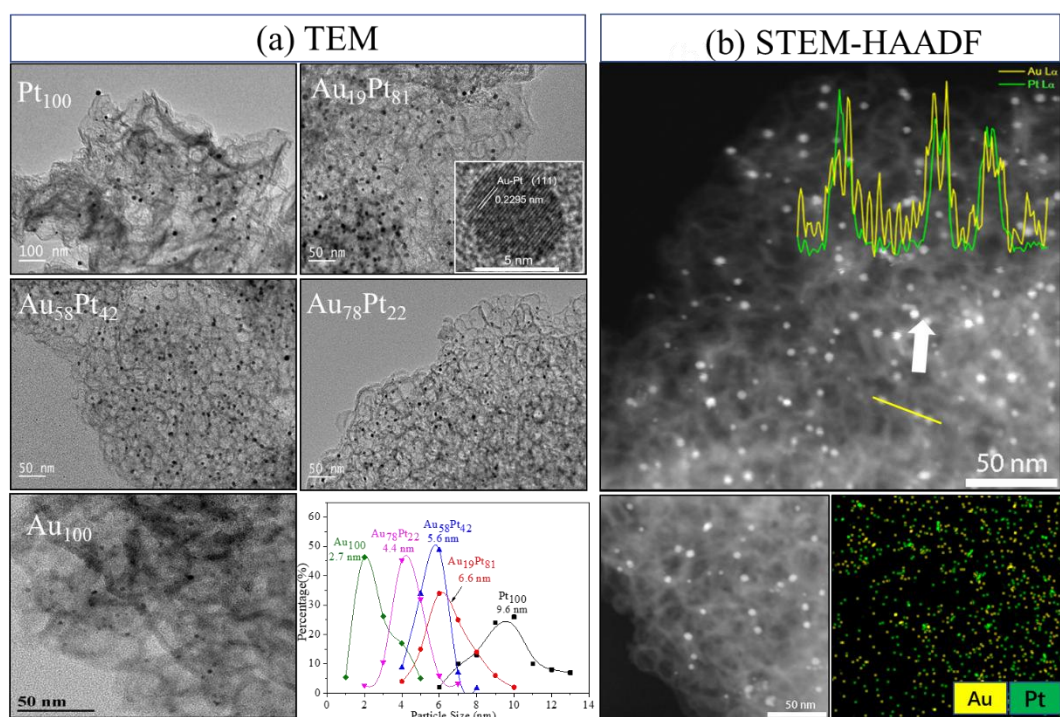


Fig. 2. (a)TEM images and particle size distribution histograms of catalysts and (b) STEM-HAADF image of sample Au₅₈Pt₄₂/MCF (Inset: energy dispersive line scan across NPs using the Pt-M and Au-M X-rays with color-coded EDS spectral maps of Pt (green) and Au (yellow)).

Well-dispersed Au-Pt bimetallic NPs were found to be supported on the foam-like mesoporous silica by TEM analysis. The STEM-HAADF analysis revealed the consistent elemental distribution within particles, which has a profound effect on the catalytic performance [58, 59]. As is shown in Fig. 2b, well-dispersed Au and Pt were observed on catalyst Au₅₈Pt₄₂/MCF except for several aggregated Pt NPs,

indicating easier agglomeration of Pt. Both the line scan (inset in Fig. 2b) and EDS mapping indicated the even distribution of Pt and Au elements, and the formation of Au-Pt alloy NPs.

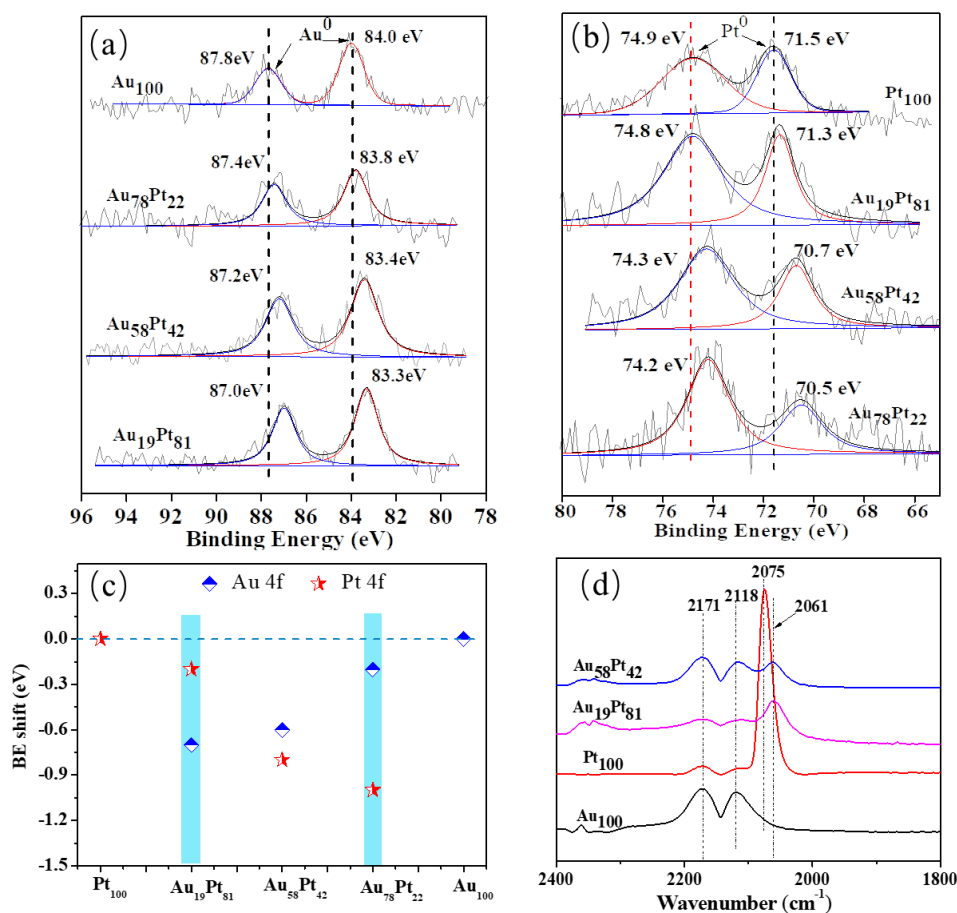


Fig. 3. (a) Au (4f) and (b) Pt (4f) XPS spectra of catalysts, (c) Au 4f and Pt 4f binding energy shifts of catalysts with different Au/Pt ratios, and (d) DRIFT spectra of CO adsorbed catalysts Au₁₀₀/MCF, Pt₁₀₀/MCF, Au₁₉Pt₈₁/MCF and Au₅₈Pt₄₂/MCF.

The Au 4f and Pt 4f XPS spectra of catalysts are shown in Fig. 3a, 3b and the binding energy shifts are indicated in Fig. 3c. The detailed bulk and surface atomic ratio are summarized in Table S2. As shown in Fig. 3a, two peaks at 84.0 eV and 87.8

eV were observed for catalyst Au₁₀₀/MCF, which are attributed to Au⁰ 4f_{7/2} (84.0 eV) and Au⁰ 4f_{5/2} (88.0 eV), respectively, indicating the presence of Au⁰ species [60-62]. With the increase of Pt loading, a negative shift of Au 4f BE to 83.3 eV (4f_{7/2}) on bimetallic catalyst Au₁₉Pt₈₁/MCF was measured. The negative shifts were also observed in Pt 4f spectra for all bimetallic catalysts (Fig. 3b). The peaks at 71.5 and 74.9 eV in the XPS spectrum of catalyst Pt₁₀₀/MCF are due to the presence of Pt⁰ species (Pt⁰ 4f_{7/2} at 71.6 eV, Pt⁰ 4f_{5/2} at 74.8 eV). While in the spectra of bimetallic catalysts, these two peaks shifted to lower BE with the increase of Au content. These negative shifts in BEs for both Au 4f and Pt 4f in Au-Pt alloy NP catalysts suggest a decrease in binding energies of Au 4f and Pt 4f electrons, which is favorable for the electron ionization or electron transfer during the reaction. The same phenomena were also observed on Au-Pt bimetallic catalysts [26, 63] and in our previous work [36]. These results reveal a variation in the electronic structure of the surface Au and Pt atoms after formation of Au-Pt alloy NPs. Previously, these negative shifts were regarded as electron transfer between Au and Pt [26] or between noble metals and support [30], resulting in the formation of negatively charged Au-Pt surface. However, this is still under debate. As is shown above, in a bimetallic Au-Pt alloy NP, the change in the electronic structure of the first metal is more evident when the content of the second metal is higher than that of the first one, (see catalysts Au₇₈Pt₂₂/MCF and Au₁₉Pt₈₁/MCF). The BE shift of Au 4f electrons is enhanced with the increase of Pt content and vice versa (Fig. 4c). In contrast to the previous elucidations, we suppose that these negative shifts of BE are closely related to the hybridization of

s-p-d orbitals [33] that cause easy release of electrons from catalyst to the adsorbent/reactants during the reaction. This explanation needs to be further clarified by other characterization techniques and theoretical calculations. In the previous work [33], a 13 atoms model was applied to reveal the essence of electronic effect on Au-Pt bimetallic catalyst, however, which is quite different with nanoparticles. A more appropriate model (such as 55 atoms model or Au, Pt, Au-Pt surfaces) should be established and applied for the calculation. Furthermore, the adsorption/desorption properties of the reactants/products on different model surfaces (Au, Pt, Au-Pt) need to be analyzed to reveal the essence of catalytic synergy.

The DRIFT spectra of CO adsorbed on catalysts Au₁₀₀/MCF, Pt₁₀₀/MCF, Au₁₉Pt₈₁/MCF and Au₅₈Pt₄₂/MCF are shown in Fig. 3d and Fig. S5 (full range spectra). The time-resolved DRIFTS spectra measured over Au₁₀₀/MCF, Pt₁₀₀/MCF and Au₅₈Pt₄₂/MCF at 25 °C under 1% CO in He are shown in Fig. S6. The reported typical CO adsorption bands over edge and corner Au sites at $\sim 2110\text{ cm}^{-1}$ and on-top CO adsorption on kinks at $\sim 2070\text{ cm}^{-1}$ was not observed [64] on catalyst Au₁₀₀/MCF, which is probably due to the strong interaction between Au NPs and silica support [29] or low CO adsorption temperature (25 °C). As shown in Fig. S6 (B, D, F), the band intensity at 2171 and 2118 cm^{-1} gradually decreased over 24 min, indicating a weak adsorption of CO on catalysts Au₁₀₀/MCF, Pt₁₀₀/MCF and Au₅₈Pt₄₂/MCF. Thus, the bands at 2171 cm^{-1} and 2118 cm^{-1} observed on all samples are ascribed to the vibration of gaseous CO [65]. The band in the region 2000-2100 cm^{-1} is usually assigned to the linearly adsorbed CO on Pt⁰ (CO-Pt⁰) [66]. An intensive CO

adsorption peak on Pt⁰ at 2075 cm⁻¹ was observed in the spectrum of catalyst Pt₁₀₀/MCF, and upon alloying with Au, a red shift of the CO absorption band from 2075 to 2061 cm⁻¹ was detected. The red shift of CO absorption band on Au and Pt for catalysts Au₁₉Pt₈₁/MCF and Au₅₈Pt₄₂/MCF is associated with the strengthened CO absorption on both Au and Pt NPs, revealing more electronic back-donation from the d orbitals of Au and Pt to the 2π* anti-bonding orbital of the adsorbed CO [67]. These results are consistent with the XPS data, indicating that more electrons are available to be donated to the adsorbent from Au and Pt in the Au-Pt alloy NPs.

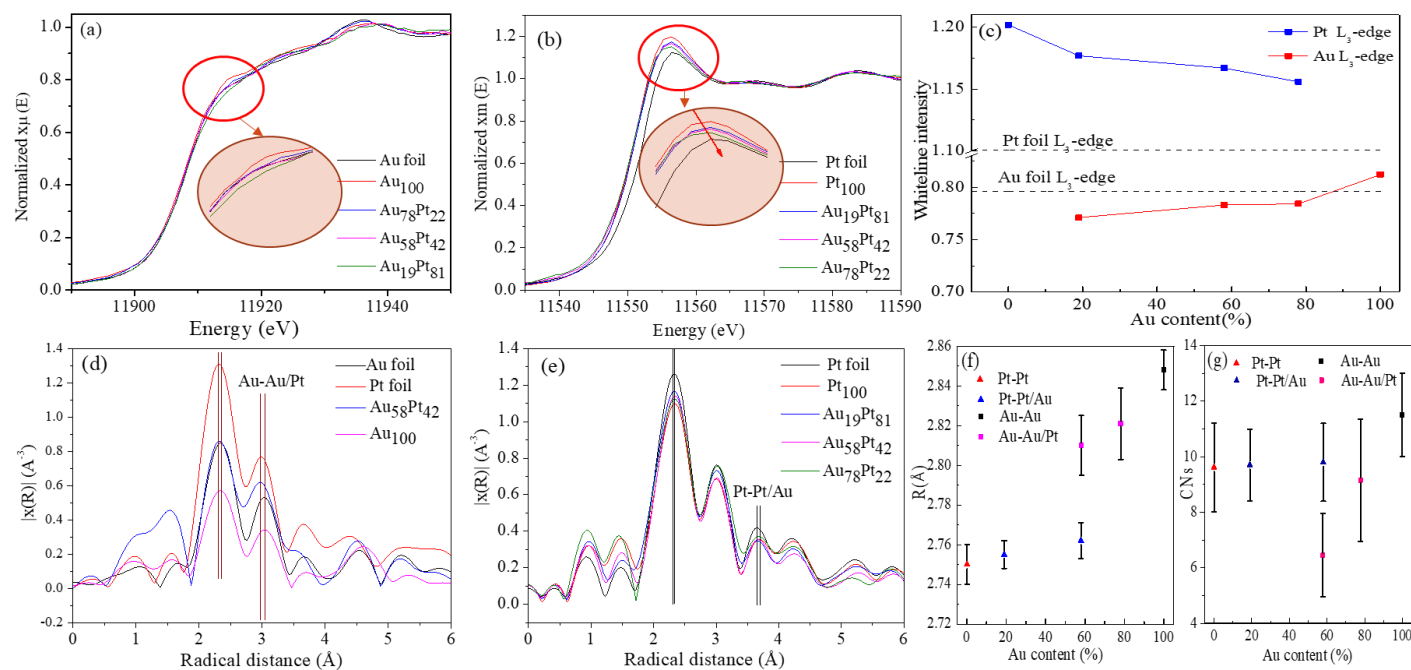


Fig. 4. Normalized (a) Au L₃-edge XANES spectra and (b) Pt L₃-edge XANES spectra; (c) White line intensity of Au L₃-edge and Pt L₃-edge XANES spectra of catalysts with different Au content. Fourier transform of EXAFS spectra of the (d) Au L₃-edge and (e) Pt L₃-edge of the monometallic and alloy catalysts along with the reference metal foil (Pt foil), (f) EXAFS fitting results of the atomic distance (R), and (g) nearest metal-metal coordination numbers (CNs) for the monometallic and Au-Pt alloy.

Normalized X-ray absorption near edge structure (XANES) spectra of Au L₃-edge and Pt L₃-edge for monometallic and alloy catalysts and the reference metal foil are shown in Fig. 4a and 4b. The white-line (WL) features in these XANES was attributed to the electron excitation from the 2p to 5d states of absorbing atom (Au and Pt) caused by X-ray, which indicates the unoccupied 5d states [26]. Theoretically, XANES spectra of Au L₃-edge exhibited no WL feature because the 5d orbitals of Au (5d¹⁰6s¹) is full. However, a small WL intensity was observed which is possibly due to the s-p-d hybridization and electron transfer from 5d to the s-p state [26]. The XANES spectra of Au L₃-edge (Fig. 4a) highlighted with red circle revealed that Pt doped with Au catalysts possess lower WL intensity than the pure Au catalyst, indicating that 5d state of Au gains electrons after doping with Pt. The positions of Pt L₃ edge XANES of samples Pt₁₀₀/MCF and bimetallic catalysts are lower than that of Pt foil in energy, implying that the Fermi level drops with diminishing of particle size of the metals. The white lines around 1157 eV of Pt₁₀₀/MCF and Au_xPt_y/MCF are higher than that of the Pt foil, indicating lower occupancy of 5d state. For Au_xPt_y/MCF catalysts, the intensity of WL decreased with increasing the Au/Pt ratio in the alloy catalysts, indicating that the 5d state of Pt atom gains electrons when doped with Au. The plots of WL intensity in Au and Pt L₃-edges XANES as a function of Au content are shown in Fig. 4c. A decreasing tendency of WL intensity in both Au and Pt L₃-edges on bimetallic catalysts were observed compare with pure Au or Pt samples, indicating that both Au and Pt 5d states gain charges in the Au-Pt alloy catalysts. The WL intensity in the Pt-L₃ edges decreased and in Au-L₃ edges increased

with the increase of Au content, indicating the electron occupancy of Au 5d and Pt 5d orbitals swing with variation of the Au/Pt ratio, which is consistent with XPS results. These results further justified our hypothesis, that electrons do not invariably transfer from one metal to another but deviate with Au/Pt ratio.

EXAFS spectra of the Au_xPt_y/MCF catalysts for the Au L_3 -edge and Pt L_3 -edge are shown in Fig. 4d, 4e along with the monometallic catalysts and reference metal foil. The fitting of EXAFS results of the bond length (R) and the nearest metal-metal coordination numbers are shown in Fig. 4f, 4g. The Au-Au/Pt distance decreased from 2.85 Å in pure Au to 2.81 Å for sample $Au_{58}Pt_{42}/MCF$, while the Pt-Pt/Au bond distance increased from 2.75 Å in pure Pt to 2.76 Å for sample $Au_{58}Pt_{42}/MCF$. The interatomic distances followed the following sequence Au-Au > Au-Pt > Pt-Pt as shown in Fig. 4f. These results indicated the contraction of Au-Au/Pt bond and expansion of Pt-Pt/Au bond, which is further revealing the formation of well-defined Au-Pt phase, the EXAFS in K and R spaces as shown in Fig. S7 and in good accordance with the XRD data.

Based on the correlation of the benzyl alcohol oxidation results with characterization of the catalysts, we could conclude that Pt is the primary active site in benzyl alcohol oxidation. The introduction of Au increased the metal dispersion through the formation of Au-Pt alloy NPs on catalysts Au_xPt_y/MCF , and also resulted in the presence of more d electrons on the surface of bimetallic alloy catalysts, leading to the enhanced catalytic activity. A close relationship between surface electron properties and catalytic activity was observed. The negative shift of Au 4f and Pt 4f

electrons BE (Fig. 3a, 3b) together with the red shift of CO absorption bands on bimetallic catalyst (Fig. 3d) indicate the increased availability of easily transferable electrons on Au and Pt atoms, which provides the direct evidence for the catalytic synergy of Au-Pt alloy catalysts. Au L₃-edge and Pt L₃-edge XANES spectra revealed that both Au and Pt 5d states gain electrons in the Au-Pt alloy NPs compared to their monometallic counterparts, which may provide transferable d electrons in valence band during the adsorption and reaction. However, the origin of these transferable electrons is still obscure. And, to date no theoretical explanation on this effect for reactants/products activation/desorption was presented.

3.3 Theoretical study

The projected density of states (PDOS) for Au and Pt atoms in the NPs using optimized 55 atoms model were calculated and shown in Fig. S8. The related primary PDOS peaks of Au and Pt atoms in Au₅₅, Pt₅₅, Au₄₀Pt₁₅ and Au₁₅Pt₄₀ NPs and the deformation electronic density map of the Au₄₀Pt₁₅ and Au₁₅Pt₄₀ NPs are shown in Fig. 5; detailed primary PDOS peaks are summarized in Table S3. The calculated PDOS peaks of the s, p, d, f states of Au atoms are lower than those of the corresponding Pt atoms in both the pure metals and alloy NPs, suggesting that the Au atoms have a stronger electron BE than the Pt atoms. After formation of Au-Pt alloy NPs, the PDOS peaks of the s, p, d, f states move up for Au and Pt atoms (Fig. 5), revealing that both the Au and Pt valence bands have been pushing toward the Fermi level. For example, the PDOS peaks of Au f and Pt f states shifted from -77.31 eV in Au₅₅ to -77.05 eV in Au₁₅Pt₄₀ and from -66.17 eV in Pt₅₅ to -65.11 eV in Au₄₀Pt₁₅ (Table S3). The upward

shift of the s, p, d, f energy level revealed that more electrons in the corresponding energy level move close to the Fermi level. The high availability of electrons near the Fermi level is usually considered to enhance surface phenomena in heterogeneous catalysis [37]. The upward shift of energy level is in good accordance with the XPS and XANES results, indicating that more electrons are available on the surface of Au-Pt alloy NPs. In the literature, these electrons were reported as electron transfer from the support or functional ligands [26, 30]. However, in this work, an increase of surface electron density on both Au and Pt atoms were observed and no electrons transfer from others was detected. Thus, the electron variation on Au-Pt bimetallic NPs was due to s-p-d hybridization and intra-atomic charge redistribution, which is probably related to the lattice structure variation as shown by XRD, TEM and EXAFS. The deformed electronic density maps of the NPs Au₁₀Pt₃ and Au₃Pt₁₀ shown in Fig. 5 indicate the rearrangement of surface electrons with different Au/Pt ratios. After the formation of Au-Pt alloy NPs, a hybridization of s-p-d orbitals occurred, electrons rearranged with different Au/Pt ratios. Further validation of these results by calculating the occupancies of s, p, d states will be provided below. In addition, the PDOS for Au and Pt atoms in Au-Pt surfaces (optimized models are shown in Fig. S9) were also calculated to eliminate the size effect, and the results are shown in Fig. S10 and Table S4. The same trend was observed for Au-Pt surface model, indicating the rationality of the calculation results.

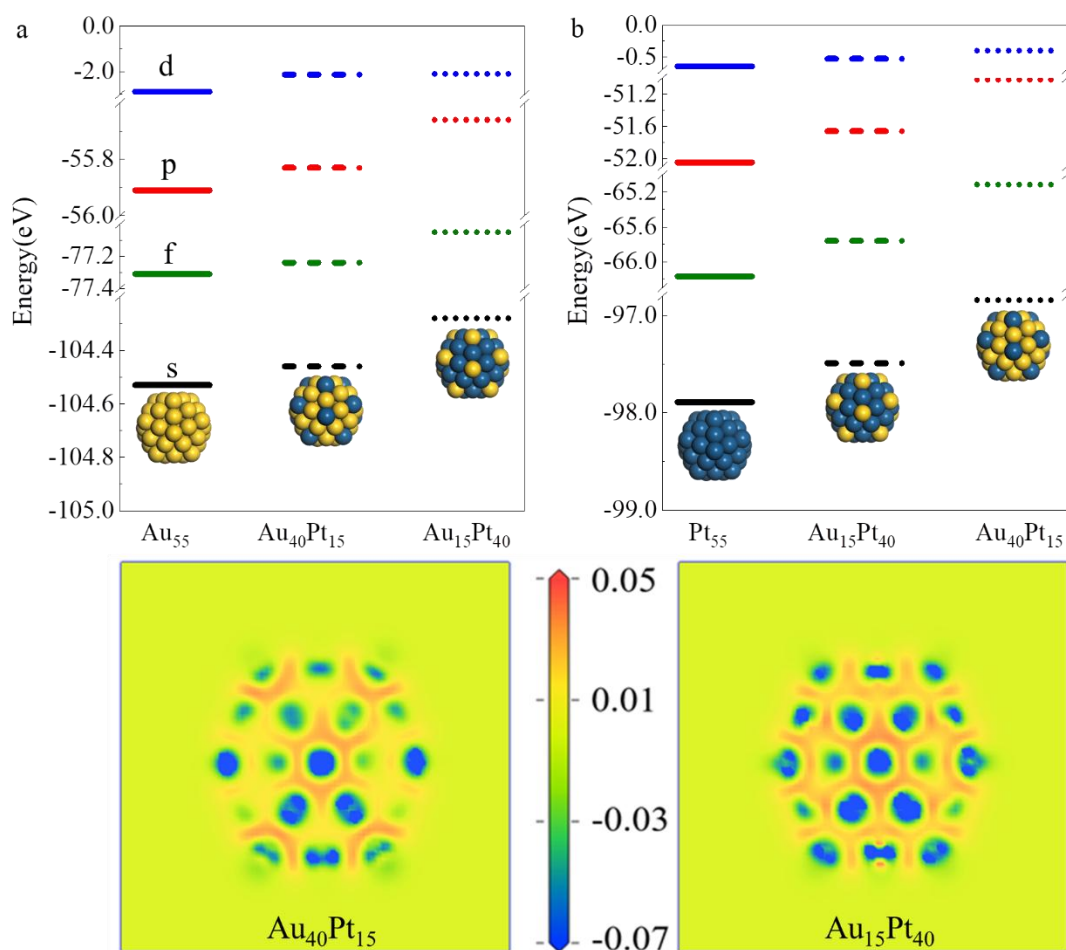


Fig. 5. The projected density of states (PDOS) of Au (a) and Pt (b) atoms in the Au_{55} , Pt_{55} , $\text{Au}_{40}\text{Pt}_{15}$ and $\text{Au}_{15}\text{Pt}_{40}$ NPs (insets: optimized models) and the deformed electronic density maps of the $\text{Au}_{40}\text{Pt}_{15}$ and $\text{Au}_{15}\text{Pt}_{40}$ NPs.

The occupancies of the 6s, 6p, 5d electrons of Au and Pt atoms in the Au_{55} , Pt_{55} , $\text{Au}_{40}\text{Pt}_{15}$ and $\text{Au}_{15}\text{Pt}_{40}$ NPs were further calculated to explore the origin of surface electrons (Table 2). The calculated total valence electrons (6s + 6p + 5d) for Au and Pt are about 11 and 10, respectively, which are in good accordance with the theoretical values, i.e. Au: $5d^{10}6s^16p^0$ and Pt: $5d^96s^16p^0$. In theory, the value of 6p electrons in Au and Pt atoms should be zero, however, on bulk Au (0.696) and bulk Pt (0.756) the 6p band is partially occupied because of orbital hybridization and electrons transfer from

5d, 6s bands to 6p. On Au₅₅ and Pt₅₅ NPs, an obvious decrease of both Au and Pt 6p electrons were observed while the amount of 6s and 5d electrons increased, which is due to the lattice shrinkage of Au/Pt after formation of NPs and electron transfer from out layer to inner layer. This is confirmed by calculating the lattice parameter of bulk and Au/Pt NPs (Table S5), which indicates that the distance d (Å) between adjacent metal atoms decreased after formation of Au (from 2.885 Å for bulk Au to 2.757 Å for Au₅₅) or Pt (from 2.775 Å for bulk Pt to 2.640 Å for Pt₅₅) NPs. Moreover, the lattice structure variation was confirmed by theoretical calculations, i.e. a lattice contraction of Au and a lattice expansion of Pt were obtained in the Au-Pt bimetallic NPs as shown in Table S5. Furthermore, an electron transfer from 6s/6p band to 5d band after the formation of Au-Pt alloy NPs was noted. Specifically, the 5d electrons of Pt increase from 8.699 (Pt₅₅) to 8.819 (Au₁₅Pt₄₀) and 8.901 (Au₄₀Pt₁₅), while the Pt 6s electrons decrease from 0.812 (Pt₅₅) to 0.776 (Au₁₅Pt₄₀) and 0.811 (Au₄₀Pt₁₅), and Pt 6p electrons decrease from 0.391 (Pt₅₅) to 0.364 (Au₁₅Pt₄₀) and 0.323 (Au₄₀Pt₁₅), indicating the electrons transfer from 6s and 6p states to 5d. These results are consistent with the XANES showing that 5d state gained charges from conduction band.

The electron occupancies of the 6s, 6p, 5d states of Au and Pt atoms in Au(111), Pt(111), AuPt₃(111) and Au₃Pt(111) surfaces were also calculated to justified the above conclusion (Table S6), the similar trend was detected. In addition, an electron density oscillation on bimetallic Au-Pt alloy NP catalyst was observed. The calculated total valence electrons (6s + 6p + 5d) on Au decreased from 11.085 (Au₄₀Pt₁₅) to

10.953 (Au₁₅Pt₄₀) with the decrease of Au content, while the total valence electrons on Pt increased from 9.995 (Au₁₅Pt₄₀) to 10.035 (Au₄₀Pt₁₅) with the decrease of Pt content, which is in accordance with XPS and XANES results. These results further indicate the presence of hybridized orbitals and intra-atomic re-distribution of electrons on Au or Pt atoms with different Au/Pt ratios, rather than simple electrons transfer from Au to Pt or vice versa.

Table 2

The occupancies (N) of the s, p, d states of Au and Pt atoms in the Au₅₅, Pt₅₅, Au₄₀Pt₁₅ and Au₁₅Pt₄₀ NPs.

State	Bulk Au	Au ₅₅	Au ₄₀ Pt ₁₅ -Au	Au ₁₅ Pt ₄₀ -Au	Au ₄₀ Pt ₁₅ -Pt	Au ₁₅ Pt ₄₀ -Pt	Pt ₅₅	Bulk Pt
6s	0.693	0.909	0.949	0.886	0.811	0.776	0.812	0.631
6p	0.696	0.433	0.462	0.401	0.323	0.364	0.391	0.756
5d	9.549	9.700	9.674	9.666	8.901	8.819	8.699	8.629
Total (s, p, d)	10.938	11.042	11.085	10.953	10.035	9.995	9.902	10.016

3.4. Reaction mechanism

Based on the above experimental and PDOS results, the presence of s-p-d hybridization and electrons re-distribution on the surface of Au or Pt atoms was confirmed. To theoretically reveal the surface properties of Au-Pt alloy NPs which are related with their catalytic activity for benzyl alcohol oxidation, DFT calculations on

Au(111), Au₃Pt(111), AuPt₃(111), and Pt(111) were performed. The adsorption and desorption properties of reactants (benzyl alcohol and O₂) and products (benzaldehyde) on the surfaces were investigated, and the charge densities of different alloy surfaces were obtained.

The adsorption/desorption configurations of benzyl alcohol, O₂, and benzaldehyde on Au (111), Au₃Pt (111), AuPt₃ (111) and Pt (111) surfaces are presented in Fig. S11, and the calculated energies are summarized in Table S7. It reveals that the improved catalytic activity of Au-Pt bimetallic NPs is not only related to adsorption energy of benzyl alcohol but most importantly to the enhanced O₂ activation on Au-Pt bimetallic surfaces. The calculated desorption energies of benzaldehyde on Au (111), Au₃Pt (111), AuPt₃(111) and Pt (111) surfaces indicate that the benzaldehyde selectivity decreases with the increase of benzaldehyde desorption energies (Table S1 and Table S7), as a result of the impeded desorption of benzaldehyde.

A good agreement between the performance of catalysts and reactants/products adsorption/desorption properties is obtained experimentally and theoretically, suggesting the significance of the adsorption property of materials on the catalytic performance. To verify this, the Hirshfeld charge population on Au(111), Au₃Pt(111), AuPt₃(111) and Pt(111) surfaces was calculated by DFT and the results are summarized in Table S8. The net charge density of the Au(111), Au₃Pt(111), AuPt₃(111) and Pt(111) surfaces are all negative, and the absolute values increase with the Pt content. The observed negative value of net charge density is consistent with

XPS and XANES results. A relation of net charge density with benzyl alcohol/O₂ adsorption energy and electron transfer is established and shown in Fig. 6. The benzyl alcohol (BA) adsorption energy increases linearly with the surface net charge density as the Pt content increases (Fig. 6a). A similar linear trend is also observed on electron transfer between BA and different catalyst surfaces, which is enhanced with the increase of surface net charge density. In addition, the electrons are found to transfer from the adsorbate (BA) to the catalyst surfaces, evidenced by their positive values. These results indicated that the net charge density of the catalyst surface is the primary factor for BA activation. The O₂ adsorption and electron transfer exhibited a different trend (Fig. 6b). It was noted that with a small amount of Au introduced, the highest adsorption energy of O₂ and the largest electron transfer from surface to O₂ are obtained on the AuPt₃(111) surface, indicating that the O₂ activation leads to formation of active intermediates (O₂^{δ-}) and this is enhanced by introducing a small amount of Au. Furthermore, the relation of catalytic activity with net charge density on different surfaces is shown in Fig. 6c. The results indicate that the more charge transfer to O₂, the higher the catalytic activity of samples was obtained. The XANES and PDOS data revealed that both Au and Pt 5d states gain charges in the Au-Pt alloy NPs, which can provide more transferable d electrons during the adsorption and the reaction. These results confirmed that the enhanced catalytic activity of Au-Pt alloy NPs was obtained through accelerating the O₂ activation (Fig. 6d).

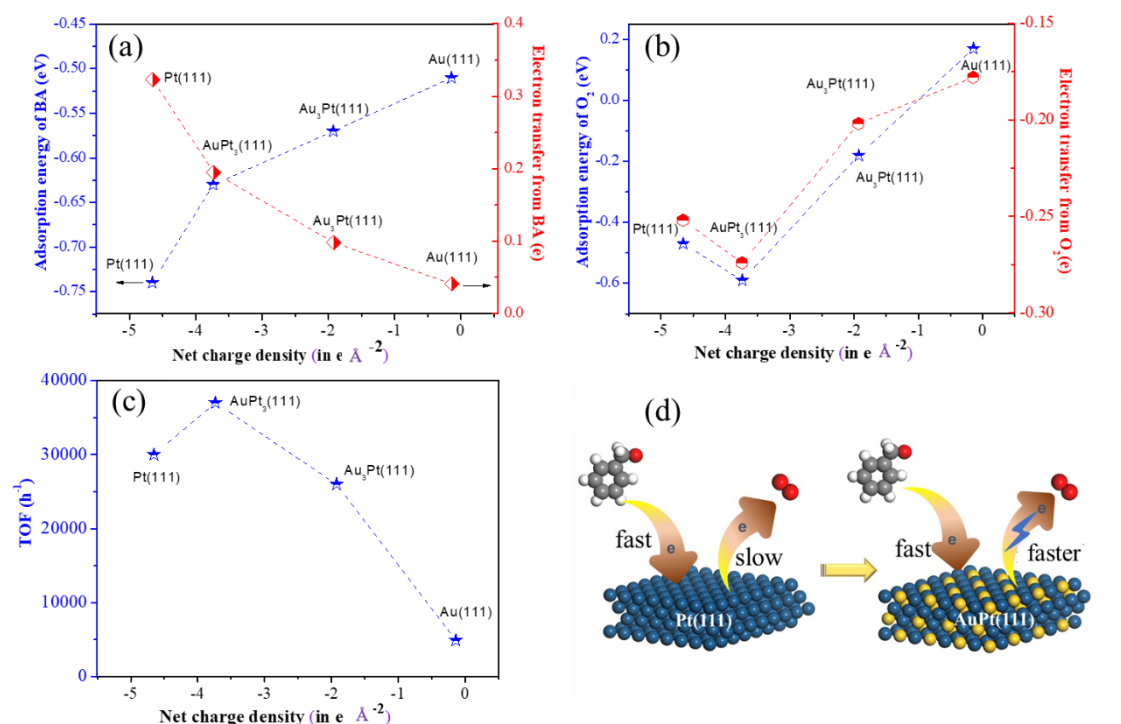
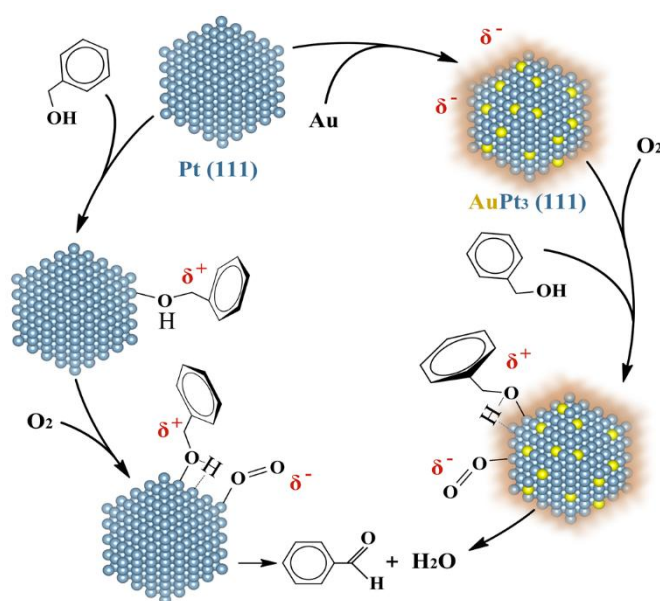


Fig. 6. Relation between net charge density and benzyl alcohol (a) and O₂ (b) adsorption energy and electron transfer on different surfaces; (c) Relation between net charge density and catalytic activity (TOF) of different surfaces and (d) electron transfer scheme of different surfaces.

To summarize, introducing a small amount of Au enhanced the electron transfer between catalyst surface and O₂, leading to a high O₂ activation capacity. This is due to the formation of Au-Pt alloy NPs that provide more transferable d electrons during the reaction as indicated by FT-IR and XANES results. Based on the experimental and theoretical results, the reaction mechanism is proposed and illustrated in Scheme 2. The benzyl alcohol adsorption is closely related to surface net charge density. In the first step, the BA is easily adsorbed on pure Pt (111) surface and a proton is abstracted from the BA to form the alkoxide. Then the O₂ was adsorbed through electrons from

Pt (111) surface to form $O_2^{\delta-}$ species, which is combined with the proton to produce H_2O . While the alkoxide undergoes structural rearrangement and desorbs as benzaldehyde. After introducing Au to Pt (111) surface, the adsorption and activation of O_2 is enhanced on $AuPt_3(111)$ surface, because more transferable d electrons can be easily donated and/or transferred to reactants. It has been previously reported that the geometric and electronic changes of the Pt sites by alloying with adjacent Au atoms can improve the catalytic activity and selectivity.[26] Hence, this phenomenon was theoretically explained herein and the essence of catalytic synergy was clarified.



Scheme 2 Reaction scheme of benzyl alcohol oxidation on Pt (111) and $AuPt_3$ (111) surfaces.

4. Conclusions

A series of Au-Pt NPs catalysts supported on mesoporous silica was designed to reveal the essence of promoter effect of Au to Pt on bimetallic catalyst. Highly dispersed Au-Pt alloy NPs supported on foam-like mesoporous silica were

obtained by a one-pot synthesis method and applied for benzyl alcohol oxidation. MCF support with developed porous structure leads to the well dispersion of noble metal NPs and eliminated the mass transfer limitation during the reaction, thus intrinsic catalytic activity was obtained. The catalytic results show that the bimetallic Au-Pt alloy NPs exhibit higher catalytic activity (TOF = 37000 h⁻¹) than the monometallic Pt (TOF = 30000 h⁻¹) and Au (TOF = 4900 h⁻¹) catalysts. The formation of Au-Pt alloy NPs resulting in the lattice structure variation was confirmed experimentally. Electronic property analyses (XPS, XANES and CO-FT-IR) identify the presence of easily transferable d electrons on Au and Pt atoms after the formation of alloy NPs. Furthermore, the theoretical PDOS results verify that the enrichment of d state electrons on Au-Pt alloy NPs is due to s-p-d hybridization and intra-atomic charge redistribution, leading to the electron transfer from 6s and 6p bands to 5d. The improved catalytic performance of the Au-Pt alloy NPs is found to be attributed to the geometric and electronic changes of the catalytically active Pt sites after introducing Au atoms. Based on the correlation between experimental and theoretical results, it is concluded that the enhanced catalytic activity is attributed to the orbital hybridization and intra-atomic electron redistribution in Au-Pt alloy NPs, leading to the increased abundance of transferable d electrons near Fermi level, which results in a high O₂ activation capacity. These results provide general theoretical guidance for the rational design of bimetallic catalysts with superior catalytic performance.

Acknowledgements

This work was supported by National Natural Science Foundation of China

(51601223, 21805307,), the National Key Technologies R & D program of China (2018YFE0118200), Shandong Provincial Natural Science Foundation (ZR2017MB003), PetroChina Innovation Foundation (2018D-5007-0504), the Fundamental Research Funds for the Central Universities (17CX05018, 17CX02056, 19CX05001A), Qingdao Postdoctoral Applied Research Project (BY20170215) and the Sino-French International Laboratory (LIA) “Zeolites”.

References

- [1] D. Huang, G.A. de Vera, C. Chu, Q. Zhu, E. Stavitski, J. Mao, H. Xin, J.A. Spies, C.A. Schmuttenmaer, J. Niu, Single-atom Pt catalyst for effective C–F bond activation via hydrodefluorination, *ACS Catal.* 8 (2018) 9353-9358.
- [2] L. Lin, S. Yao, R. Gao, X. Liang, Q. Yu, Y. Deng, J. Liu, M. Peng, Z. Jiang, S. Li, A highly CO-tolerant atomically dispersed Pt catalyst for chemoselective hydrogenation, *Nat. Nanotechnol.* 14(2019) 354–361.
- [3] Q. Liu, Y. Xu, X. Qiu, C. Huang, M. Liu, Chemoselective hydrogenation of nitrobenzenes activated with tuned Au/h-BN, *J. Catal.* 370 (2019) 55-60.
- [4] L. Ye, X. Duan, S. Wu, T.-S. Wu, Y. Zhao, A.W. Robertson, H.-L. Chou, J. Zheng, T. Ayvali, S. Day, Self-regeneration of Au/CeO₂ based catalysts with enhanced activity and ultra-stability for acetylene hydrochlorination, *Nat. Commun.* 10 (2019) 914-924.
- [5] D.-H. Kim, S.-J. Kim, H. Shin, W.-T. Koo, J.-S. Jang, J.-Y. Kang, Y.J. Jeong, I.-D. Kim, High-resolution, fast, and shape-conformable hydrogen sensor platform: polymer nanofiber yarn coupled with nano-grained Pd@ Pt, *ACS nano* 13 (2019)

6071-6082.

[6] S. Zhang, M. Yang, K. Liang, A. Turak, B. Zhang, D. Meng, C. Wang, F. Qu, W. Cheng, M. Yang, An acetone gas sensor based on nanosized Pt-loaded Fe_2O_3 nanocubes, *Sensors and Actuat. B: Chem.* 290 (2019) 59-67.

[7] S.-i. Yamazaki, M. Asahi, T. Ioroi, Promotion of oxygen reduction on a porphyrine-modified Pt catalyst surface, *Electrochim. Acta* 297 (2019) 725-734.

[8] Y. Nie, L. Li, Z. Wei, Recent advancements in Pt and Pt-free catalysts for oxygen reduction reaction, *Chem. Soc. Rev.* 44 (2015) 2168-2201.

[9] J. Choi, J. Cho, C.-W. Roh, B.-S. Kim, M.S. Choi, H. Jeong, H.C. Ham, H. Lee, Au-doped PtCo/C catalyst preventing Co leaching for proton exchange membrane fuel cells, *Appl. Catal. B: Environ.* 247 (2019) 142-149.

[10] Q. Lv, H. Min, D.B. Duan, W. Fang, G.M. Pan, A.G. Shen, Q.Q. Wang, G. Nie, J.M. Hu, Total aqueous synthesis of Au@ Cu_{2-x}S core-shell nanoparticles for In Vitro and In Vivo SERS/PA imaging- guided photothermal cancer therapy, *Adv. Healthcare Mater.* 8 (2019) 1801257-1801268.

[11] H. Wen, H. Wang, J. Hai, S. He, F. Chen, B. Wang, Photochemical synthesis of porous $\text{CuFeSe}_2/\text{Au}$ heterostructured nanospheres as SERS sensor for ultrasensitive detection of lung cancer cells and their biomarkers, *ACS Sustainable Chem. Eng.* (2019), DOI: 10.1021/acssuschemeng.8b06116.

[12] A. Taketoshi, M. Haruta, Size-and structure-specificity in catalysis by gold clusters, *Chem. Lett.* 43 (2014) 380-387.

[13] J. Pritchard, M. Piccinini, R. Tiruvalam, Q. He, N. Dimitratos, J.A.

Lopez-Sanchez, D.J. Morgan, A.F. Carley, J.K. Edwards, C.J. Kiely, Effect of heat treatment on Au–Pd catalysts synthesized by sol immobilisation for the direct synthesis of hydrogen peroxide and benzyl alcohol oxidation, *Catal. Sci. Technol.* 3 (2013) 308-317.

[14] C.P. Ferraz, M. Zieliński, M. Pietrowski, S. Heyte, F. Dumeignil, L.M. Rossi, R. Wojcieszak, Influence of support basic sites in green oxidation of biobased substrates using Au-promoted catalysts, *ACS Sustainable Chem. Eng.* 6 (2018) 16332-16340.

[15] S. Campisi, M. Ferri, C.E. Chan-Thaw, F.J. Sanchez Trujillo, D. Motta, T. Tabanelli, N. Dimitratos, A. Villa, Metal-support cooperative effects in Au/VPO for the aerobic oxidation of benzyl alcohol to benzyl benzoate, *Nanomaterials* 9 (2019) 299-314.

[16] S.K. Mehta, S. Gupta, Synthesis of Au-Pd alloy nanoparticles and their catalytic activity in the electrooxidation of formic acid and lower alcohols in alkaline media, *Sci. Adv. Mater.* 5 (2013) 1377-1383.

[17] S.L. Ming Yang, Yuan Wang, Jeffrey A. Herron, Ye Xu, Lawrence F. Allard, Sungsik Lee, Jun Huang, Manos Mavrikakis, Maria Flytzani-Stephanopoulos,, Catalytically active Au-O(OH)^{x-} species stabilized by alkali ions on zeolites and mesoporous oxides, *Science* 346 (2014) 1498-1501.

[18] J. Xin, H. Fan, S. Ji, Y. Wang, C. Xia, Methanobactin-mediated synthesis of bimetallic Au-Pd/Al₂O₃ toward an efficient catalyst for glucose oxidation, *Iet Nanobiotechnology* 11 (2017) 512-516.

[19] J. Li, B. Zhu, G. Wang, Z. Liu, WHuang, S. Zhang, Enhanced CO catalytic

oxidation over an Au-Pt alloy supported on TiO₂ nanotubes: investigation of the hydroxyl and Au/Pt ratio influences, *Catal. Sci. Technol.* 8 (2018) 6109-6122.

[20] H. Li, W. Chai, G. Henkelman, Selectivity for ethanol partial oxidation: The unique chemistry of single-atom alloy catalysts on Au, Ag, and Cu (111), *J Mater. Chem. A* 7 (2019) 23868-23877.

[21] P. Wu, P. Bai, Z. Yan, G.X. Zhao, Gold nanoparticles supported on mesoporous silica: origin of high activity and role of Au NPs in selective oxidation of cyclohexane, *Sci. Rep.* 6 (2016) 18817-18828.

[22] J. Mai, Y. Fang, J. Liu, J. Zhang, X. Cai, Y. Zheng, Simple synthesis of WO₃-Au composite and their improved photothermal synergistic catalytic performance for cyclohexane oxidation, *Mol. Catal.* 473 (2019) 110389-110396.

[23] R.D. Armstrong, J. Hirayama, D.W. Knight, G.J. Hutchings, Quantitative determination of Pt-catalyzed D-glucose oxidation products using 2D NMR, *ACS Catal.* 9 (2018) 325-335.

[24] W.C. Ho, K. Chung, A.J. Ingram, R.M. Waymouth, Pd-Catalyzed aerobic oxidation reactions: strategies to increase catalyst lifetimes, *J. Am. Chem. Soc.* 140 (2018) 748-757.

[25] C.M. Olmos, L.E. Chinchilla, A. Villa, J.J. Delgado, A.B. Hungría, G. Blanco, L. Prati, J.J. Calvino, X. Chen, Size, nanostructure, and composition dependence of bimetallic Au-Pd supported on ceria-zirconia mixed oxide catalysts for selective oxidation of benzyl alcohol, *J. Catal.* 375 (2019) 44-55.

[26] S.N. Duangta Tongsakul, and Kohki Ebitani, Platinum/Gold alloy

nanoparticles-supported hydrotalcite catalyst for selective aerobic oxidation of polyols in base-free aqueous solution at room temperature, *ACS Catal.* (2013) 2199-2207.

[27] A. Savara, C.E. Chan-Thaw, J.E. Sutton, D. Wang, L. Prati, A. Villa, Molecular origin of the selectivity differences between palladium and gold-palladium in benzyl alcohol oxidation: different oxygen adsorption properties, *Chemcatchem* 9 (2017) 253-257.

[28] J.H. Carter, S. Althahban, E. Nowicka, S.J. Freakley, D.J. Morgan, P.M. Shah, S. Golunski, C.J. Kiely, G.J. Hutchings, Synergy and anti-synergy between palladium and gold in nanoparticles dispersed on a reducible support, *ACS Catal.* 6 (2016) 6623-6633.

[29] P. Wu, Y. Cao, L. Zhao, Y. Wang, Z. He, W. Xing, P. Bai, S. Mintova, Z. Yan, Formation of PdO on Au–Pd bimetallic catalysts and the effect on benzyl alcohol oxidation, *J. Catal.* 375 (2019) 32-43.

[30] R.J. Wong, J. Scott, P. Kappen, G.K.C. Low, J.N. Hart, R. Amal, Enhancing bimetallic synergy with light: the effect of UV light pre-treatment on catalytic oxygen activation by bimetallic Au-Pt nanoparticles on a TiO₂ support, *Catal. Sci. Technol.* 7 (2017) 4792-4805.

[31] M. Mounquengui-Diallo, F. Vermersch, N. Perret, C. Pinel, M. Besson, Base free oxidation of 1,6-hexanediol to adipic acid over supported noble metal mono- and bimetallic catalysts, *Appl. Catal. A-Gen.* 551 (2018) 88-97.

[32] D. Tongsakul, S. Nishimura, K. Ebitani, Platinum/gold alloy nanoparticles-supported hydrotalcite catalyst for selective aerobic oxidation of polyols

- in base-free aqueous solution at room temperature, *ACS Catal.* 3 (2013) 2199-2207.
- [33] E. Bus, J.A. van Bokhoven, Electronic and geometric structures of supported platinum, gold, and platinum–gold catalysts, *J Phys. Chem. C* 111 (2007) 9761-9768.
- [34] J. A. Herron, M. Mavrikakis. On the composition of bimetallic near-surface alloys in the presence of oxygen and carbon monoxide. *Catal Comm* 52 (2014), 65-71.
- [35] D. Wang, X. Cui, Q. Xiao, Y. Hu, Z. Wang, Y. Yiu, T. Sham, Electronic behaviour of Au-Pt alloys and the 4f binding energy shift anomaly in Au bimetallics-X-ray spectroscopy studies, *AIP Advances* 8 (2018) 065210.
- [36] P. Wu, Y. Cao, Y. Wang, W. Xing, Z. Zhong, P. Bai, Z. Yan, Ultrastable bimetallic catalyst with tuned surface electronic properties for highly selective oxidation of cyclohexane, *Appl. Surf. Sci.* 457 (2018) 580-590.
- [37] L.D. Germano, V.S. Marangoni, N.V.V. Mogili, L. Seixas, C.M. Maroneze, Ultrasmall (<2 nm) Au@Pt nanostructures: Tuning the surface electronic states for electrocatalysis, *ACS Appl. Mater. Interf.* 11 (2019) 5661-5667.
- [38] J. Kim, R. J. Desch, S. W. Thiel , V. V. Gulians, N. G. Pinto, Adsorption of biomolecules on mesostructured cellular foam silica: Effect of acid concentration and aging time in synthesis. *Micropor. Mesopor. Mat.* 149 (2012) 60–68.
- [39] M. López- Haro, J.J. Delgado, J.M. Cies, E. del Rio, S. Bernal, R. Burch, M.A. Cauqui, S. Trasobares, J.A. Pérez- Omil, P. Bayle- Guillemaud, Bridging the gap between CO adsorption studies on gold model surfaces and supported nanoparticles, *Angew. Chem. Int. Ed.* 49 (2010), 1981-1985.

- [40] Y. Du, Y. Zhu, S. Xi, P. Yang, H.O. Moser, M.B.H. Breese, A. Borgna, XAFCA: a new XAFS beamline for catalysis research, *J Synchrotron Radiat.* 22 (2015) 839-843.
- [41] B. Ravel, M. Newville, ATHENA, ARTEMIS, HEPHAESTUS: data analysis for X-ray absorption spectroscopy using IFEFFIT, *J Synchrotron Radiat.* 12 (2005) 537-541.
- [42] B. Delley, An all- electron numerical method for solving the local density functional for polyatomic molecules, *J Chem. Phys.* 92 (1990) 508-517.
- [43] B. Delley, Fast calculation of electrostatics in crystals and large molecules, *J Phys. Chem.* 100 (1996) 6107-6110.
- [44] J.P. Perdew, K. Burke, M. Ernzerhof, Generalized gradient approximation made simple, *Phys. Rev. Lett.* 77 (1996) 3865-3875.
- [45] S. Grimme, Semiempirical GGA- type density functional constructed with a long- range dispersion correction, *J. Comput. Chem.* 27 (2006) 1787-1799.
- [46] Z. Wu, L. Xu, W. Zhang, Y. Ma, Q. Yuan, Y. Jin, J. Yang, W. Huang, Structure sensitivity of low-temperature NO decomposition on Au surfaces, *J. Catal.* 304 (2013) 112-122.
- [47] M. Segall, P.J. Lindan, M.a. Probert, C.J. Pickard, P.J. Hasnip, S. Clark, M. Payne, First-principles simulation: ideas, illustrations and the CASTEP code, *J. Phys.: Condens. Matter.* 14 (2002) 2717-2744.
- [48] C.J. Pickard, On-the-fly pseudopotential generation in CASTEP, School of Physics and Astronomy, University of St Andrews St Andrews, KY16 9SS, United Kingdom, (2006).

- [49] D.E. Mears, Tests for transport limitations in experimental catalytic reactors, *Ind. Eng. Chem. Process. Des. Dev.* 10 (1971) 541.
- [50] G.N. Yun, S.J. Ahn, A. T. R. Kikuchi, S. T. Oyama, Hydrodeoxygenation of ϵ -valerolactone on bimetallic NiMo phosphide catalysts, *J. Catal.* 353 (2017) 141–151
- [51] S.T. Oyama, X. Zhang, J. Lu, Y. Gu, T. Fujitani, Epoxidation of propylene with H_2 and O_2 in the explosive regime in a packed-bed catalytic membrane reactor, *J. Catal.* 257 (2008) 1–4.
- [52] J. Sa, S.F.R. Taylor, H. Daly, A. Goguet, R. Tiruvalam, Q. He, C.J. Kiely, G.J. Hutchings, C. Hardacre, Redispersion of gold supported on oxides, *ACS Catal.* 2 (2012) 552-560.
- [53] P. Wu, Z. Xiong, K.P. Loh, X. Zhao, Selective oxidation of cyclohexane over gold nanoparticles supported on mesoporous silica prepared in the presence of thioether functionality, *Catal. Sci. Technol.* 1 (2011) 285-294.
- [54] K. A. Cychosz, R. Guillet-Nicolas, J. Garcia-Martinez and M. Thommes Recent advances in the textural characterization of hierarchically structured nanoporous materials, *Chem. Soc. Rev.* 46 (2017) 389-414.
- [55] M. Thommes, B. Smarsly, M. Groenewolt, P. O. Ravikovitch, A. V. Neimark, Cavitation in Metastable Liquid Nitrogen Confined to Nanoscale Pores. *Langmuir* 22 (2006) 756-764.
- [56] M. Thommes, K. Kaneko, A. V. Neimark, J. P. Olivier, F. Rodriguez-Reinoso, J. Rouquerol, K. S. W. Sing, Physisorption of gases, with special reference to the

evaluation of surface area and pore size distribution (IUPAC Technical Report), *Pure Appl. Chem.* 87 (2015) 1051–1069.

[57] T. Mallat, A. Baiker, Oxidation of alcohols with molecular oxygen on solid catalysts, *Chem. Rev.* 104 (2004) 3037-3058.

[58] C.M. Olmos, L.E. Chinchilla, A. Villa, J.J. Delgado, H. Pan, A.B. Hungria, G. Blanco, J.J. Calvino, L. Prati, X. Chen, Influence of pretreatment atmospheres on the performance of bimetallic Au-Pd supported on ceria-zirconia mixed oxide catalysts for benzyl alcohol oxidation, *Appl. Catal. A-Gen.* 525 (2016) 145-157.

[59] R. Tiruvalam, J. Pritchard, N. Dimitratos, J. Lopez-Sanchez, J. Edwards, A. Carley, G. Hutchings, C. Kiely, Aberration corrected analytical electron microscopy studies of sol-immobilized Au⁺ Pd, Au {Pd} and Pd {Au} catalysts used for benzyl alcohol oxidation and hydrogen peroxide production, *Faraday Discuss.* 152 (2011) 63-86.

[60] A. Venezia, V. La Parola, V. Nicoli, G. Deganello, Effect of gold on the HDS activity of supported palladium catalysts, *J. Catal.* 212 (2002) 56-62.

[61] S. Deki, K. Akamatsu, Y. Hatakenaka, M. Mizuhata, A. Kajinami, Synthesis and characterization of nano-sized gold-palladium bimetallic particles dispersed in polymer thin film matrix, *Nanostruct. Mater.* 11 (1999) 59-65.

[62] A. Venezia, L. Liotta, G. Pantaleo, V. La Parola, G. Deganello, A. Beck, Z. Koppány, K. Frey, D. Horvath, L. Guzzi, Activity of SiO₂ supported gold-palladium catalysts in CO oxidation, *Appl. Catal. A-Gen.* 251 (2003) 359-368.

[63] J. Long, H. Liu, S. Wu, S. Liao, Y. Li, Selective oxidation of saturated

hydrocarbons using Au-Pd alloy nanoparticles supported on metal-organic frameworks, *ACS Catal.* 3 (2013) 647-654.

[64] R. Atwi, T. Elgayyar, F. J. C. S. Aires, A. Tuel and F. C. Meunier, Revisiting the evolution of IR spectra of CO adsorbed on Au nanoparticles supported on non-reducible supports. *Top. Catal.*, (2020)
<https://doi.org/10.1007/s11244-020-01372-2>.

[65] Y. Wu, L. Tan, T. Zhang, H. Xie, G. Yang, N. Tsubaki, J. Chen, Effect of preparation method on ZrO₂-based catalysts performance for isobutanol synthesis from syngas, *Catalysts* 9 (2019) 752.

[66] Y.W. Shaofeng Song, Shasha Ge, Li Wang, Yunsong Wang, Yanglong Guo, Wangcheng Zhan, and Yun Guo, A facile way to improve Pt atom efficiency for CO oxidation at low temperature: modification by transition metal oxides, *ACS Catal.* 9 (2019) 6177-6187.

[67] L. Ouyang, G.-j. Da, P.-f. Tian, T.-y. Chen, J. Xu, Y.-F. Han, Insight into active sites of Pd–Au/TiO₂ catalysts in hydrogen peroxide synthesis directly from H₂ and O₂, *J. Catal.* 311 (2014) 129-136.